



# A thioether-decorated triazine-based covalent organic framework towards overall H<sub>2</sub>O<sub>2</sub> photosynthesis without sacrificial agents

Zhiming Zhou<sup>a,b</sup>, Minghui Sun<sup>c</sup>, Yanbin Zhu<sup>a</sup>, Peize Li<sup>a</sup>, Yanrong Zhang<sup>c,\*</sup>, Mingkui Wang<sup>a</sup>, Yan Shen<sup>a,\*</sup>

<sup>a</sup> Wuhan National Laboratory for Optoelectronics, Huazhong University of Science and Technology, Luoyu Road 1037, Wuhan, Hubei 430074, PR China

<sup>b</sup> Key Laboratory of Material Chemistry for Energy Conversion and Storage, Ministry of Education, School of Chemistry and Chemical Engineering, Huazhong University of Science and Technology, Luoyu Road 1037, Wuhan, Hubei 430074, PR China

<sup>c</sup> School of Environmental Science and Engineering, Huazhong University of Science and Technology, Luoyu Road 1037, Wuhan, Hubei 430074, PR China

## ARTICLE INFO

### Keywords:

Overall H<sub>2</sub>O<sub>2</sub> photosynthesis  
Covalent organic frameworks  
Thioether  
Band structure regulation  
Two-electron pathway

## ABSTRACT

Covalent organic frameworks (COFs) have been rapidly applied in photocatalytic H<sub>2</sub>O<sub>2</sub> production owing to their strong light absorption, suitable band structure, etc. However, sluggish water oxidation reaction (WOR) with low selectivity restricts the H<sub>2</sub>O<sub>2</sub> photosynthesis efficiency of COFs. Herein, a thioether-decorated triazine-based COF (TDB-COF) was designed and developed for efficient overall H<sub>2</sub>O<sub>2</sub> photosynthesis. TDB-COF achieves a photocatalytic H<sub>2</sub>O<sub>2</sub> production rate of 723.5 μmol g<sup>-1</sup> h<sup>-1</sup> without any sacrificial agents and exhibits remarkable cyclic stability. The modification of thioether groups broadens the visible light absorption of TDB-COF and narrows its optical band gap. Such a strategy can not only effectively regulate the band structure suitable for two-electron two-steps WOR but also promote the photogenerated carriers transfer and accelerate a two-electron two-steps oxygen reduction process to generate H<sub>2</sub>O<sub>2</sub>, thus ultimately boosting the overall H<sub>2</sub>O<sub>2</sub> photosynthesis. This work provides valuable suggestions for the development of the functional COFs towards overall H<sub>2</sub>O<sub>2</sub> photosynthesis.

## 1. Introduction

Hydrogen peroxide (H<sub>2</sub>O<sub>2</sub>) is an environment friendly chemical used widely in various of industries [1–4]. Common methods for H<sub>2</sub>O<sub>2</sub> synthesis, including anthraquinone process, electrochemical method and oxidation of alcohols, are not only waste-intensive and expensive but also have some inevitable problems such as complicated multistep reactions and large consumption of organic solvents [5–7]. Meanwhile, from the point view of large-scale industrialization, a direct synthesis of H<sub>2</sub>O<sub>2</sub> from H<sub>2</sub> and O<sub>2</sub> by using noble metals catalysts is extremely dangerous because of the explosive nature of H<sub>2</sub>/O<sub>2</sub> mixture [8,9]. Therefore, it is highly significant to further develop cleaner and more efficient approaches for H<sub>2</sub>O<sub>2</sub> synthesis. Photocatalytic H<sub>2</sub>O<sub>2</sub> production directly from H<sub>2</sub>O and O<sub>2</sub> through water oxidation reaction (WOR) and oxygen reduction reaction (ORR) is an environmentally sustainable and alternative technology because of its low-cost, non-toxicity, safety and high-efficiency [10–12]. Photocatalytic strategy combining WOR with ORR to generate H<sub>2</sub>O<sub>2</sub> is one of the most potential routes [13]. Overall H<sub>2</sub>O<sub>2</sub> photosynthesis can be achieved by two routes for WOR and two

routes for ORR [14]. The photocatalytic WOR routes to generate H<sub>2</sub>O<sub>2</sub> consist of a direct 2e<sup>-</sup> one-step process (Eq. (1)) or a 2e<sup>-</sup> two-steps process with ·OH as the intermediate species (Eqs. (2) and (3)). Besides, the photocatalytic ORR routes to produce H<sub>2</sub>O<sub>2</sub> include a direct 2e<sup>-</sup> one-step reaction (Eq. (4)) or a 2e<sup>-</sup> two-steps process combining H<sup>+</sup> (Eqs. (5) and (6)) [15].



Covalent organic frameworks (COFs) are an emerging class of organic photocatalysts, which are constructed from pre-designable

\* Corresponding authors.

E-mail addresses: [yanrong.zhang@hust.edu.cn](mailto:yanrong.zhang@hust.edu.cn) (Y. Zhang), [ciac\\_sheny@mail.hust.edu.cn](mailto:ciac_sheny@mail.hust.edu.cn) (Y. Shen).

<https://doi.org/10.1016/j.apcatb.2023.122862>

Received 9 February 2023; Received in revised form 2 May 2023; Accepted 6 May 2023

Available online 7 May 2023

0926-3373/© 2023 Elsevier B.V. All rights reserved.

building blocks via strong covalent bonds [16–20]. More recently, COFs have been rapidly developed in photocatalytic  $\text{H}_2\text{O}_2$  production owing to their flexible and controllable topology, ordered crystalline structure, remarkable light absorption, and plentiful redox active sites, *etc* [21–26]. Especially, metal-free triazine-based COFs are efficient photocatalysts for  $\text{H}_2\text{O}_2$  photosynthesis by the  $2\text{e}^-$  ORR [27,28]. For instance, Han et al. reported a fluorine-substituted triazine COF, which widens the visible-light absorption range and boosts charge separation and transfer, ultimately promoting a  $2\text{e}^-$  two-steps ORR process for enhanced photocatalytic  $\text{H}_2\text{O}_2$  production [29]. However, the  $2\text{e}^-$  WOR of the  $\text{H}_2\text{O}_2$  photosynthesis over COFs faces limited activity and poor selectivity, which further seriously restricts the photocatalytic  $\text{H}_2\text{O}_2$  production efficiency. Notably, the modification of thioether functionalization can promote the visible-light response and effectively tune the band structure of triazine-based COFs, which is beneficial for the photogenerated carrier separation and charge transport [30]. Therefore, the newly developed triazine-based COFs with functional thioether moiety and abundant active sites can be highly promising for photocatalytic  $\text{H}_2\text{O}_2$  production.

In this work, we construct and develop a thioether-decorated triazine-based COF (TDB-COF) via a multicomponent strategy towards the overall  $\text{H}_2\text{O}_2$  photosynthesis from  $\text{H}_2\text{O}$  and  $\text{O}_2$  without any sacrificial agents or cocatalysts. The ordered thioether groups in the structure of TDB-COF can effectively improve the light absorption capacity and adjust the energy band structure, which is beneficial for enhanced photocatalytic  $\text{H}_2\text{O}_2$  production. Consequentially, the thioether-containing TDB-COF can sustainably achieve photocatalytic activity with a  $\text{H}_2\text{O}_2$  production rate of  $723.5 \mu\text{mol g}^{-1} \text{h}^{-1}$  without any sacrificial agents or cocatalysts and exhibit remarkable cyclic stability. Furthermore, TDB-COF maintains its chemical structure stability after photocatalytic cycling reaction. The introduction of thioether groups can not only broaden the visible-light absorption of TDB-COF and regulate its band structure suitable for  $2\text{e}^-$  two-steps WOR to produce  $\text{H}_2\text{O}_2$  but also accelerate a  $2\text{e}^-$  two-steps ORR process, thus ultimately achieving overall  $\text{H}_2\text{O}_2$  photosynthesis. This work provides some important indications for the design and development of metal-free COFs towards chemical fuels photosynthesis from  $\text{H}_2\text{O}$  and air.

## 2. Experimental section

### 2.1. Preparation of COFs photocatalyst

TDB-COF was designed based on a multicomponent strategy [17] and prepared by using different functional monomers, including 4,4', 4''-(1,3,5-triazine-2,4,6-triyl)tribenzaldehyde (TFPT), thioether-containing 2,5-bis(2-(ethylthio)ethoxy)terephthalohydrazide (BETH), and 2,5-diethoxyterephthalohydrazide (DETH). TFPT (15.0 mg,  $38.13 \mu\text{mol}$ ), BETH (15.4 mg,  $38.13 \mu\text{mol}$ ), and DETH (5.4 mg,  $19.07 \mu\text{mol}$ ) were dissolved in dioxane/mesitylene solution (1:3 v/v, 1.0 mL) and 6.0 M aqueous acetic acid (0.2 mL) at room temperature, which was sonicated for 10 min. The above mixed system was degassed by three freeze-pump-thaw cycles, and then the Pyrex tube was flame sealed. After cooled to room temperature, the Pyrex tube was placed in an oven at  $120^\circ\text{C}$  for 3 days yielding a yellow powder. The precipitate was collected by filtration, washed with anhydrous THF and acetone. The resultant yellow powder was dried at  $80^\circ\text{C}$  under vacuum overnight to yield the photocatalyst (TDB-COF). For comparison, TFPT-COF was prepared according to the same method.

### 2.2. Photocatalytic $\text{H}_2\text{O}_2$ production

10 mL deionized water containing 10 mg of photocatalyst was sonicated for 3 min and stirring in ice water bath and under the dark conditions for 1 h. Then the above system was irradiated and vigorously stirred at 273 K. The simulated AM 1.5 G illumination was chosen as illuminated light source. No sacrificial agent or cocatalyst was needed.

The photocatalytic experiment was performed under different atmospheric conditions ( $\text{Ar}/\text{Air}/\text{O}_2$ ). During the photocatalytic process, an aliquot was taken from the mixture at given time intervals, and filtrated to remove the photocatalyst. The concentration of  $\text{H}_2\text{O}_2$  generated from the photocatalytic reaction was determined by potassium permanganate titration method and spectrophotometric method with potassium titanium oxalate. After the photocatalytic process, the photocatalyst was recycled by the centrifugation, washing and drying, and used for next cyclic reaction.

### 2.3. Apparent quantum yield measurements

The apparent quantum yield (AQY) as a function of light absorption spectra can be calculated from the following formula [31]:

$$\text{AQY} = \frac{2 \times n_{\text{H}_2\text{O}_2} \times N_A}{N}$$

$n_{\text{H}_2\text{O}_2}$  is the number of evolved  $\text{H}_2\text{O}_2$  molecules,  $N_A$  is Avogadro number ( $6.02 \times 10^{23}$ ) and  $N$  represents the number of incident photons, which can be calculated from the following equation:

$$N = \frac{\text{light intensity}(\text{Wcm}^{-2}) \times \text{illumination area}(\text{cm}^2)}{\frac{hc}{\lambda}}$$

$h$  is plank constant ( $6.626 \times 10^{-34} \text{ J s}$ ),  $c$  is the speed of light ( $3.0 \times 10^8 \text{ m s}^{-1}$ ),  $\lambda$  is the wavelength of light (365, 400, 550 and 650 nm). The irradiated area is  $6.4 \text{ cm}^2$ . The photocatalytic system with 10 mg catalyst and 10 mL  $\text{O}_2$  saturated water was irradiated for 1 h at room temperature under atmospheric pressure without any sacrificial agents or cocatalysts.

### 2.4. Electrochemical measurements

Electrochemical measurements of the photocatalysts were performed on a standard three-electrode system by an electrochemical workstation (CHI-660D, Shanghai Chenhua, China). The resulting electrode, twisted platinum wire and Ag/AgCl electrode were used as working, counter and reference electrodes, respectively. The 0.5 M  $\text{Na}_2\text{SO}_4$  aqueous solution ( $\text{pH} = 7$ ) was chosen as supporting electrolyte. High purity nitrogen was purged into the system for 30 min before electrochemical tests. Electrochemical impedance spectroscopy (EIS) curves were recorded in the frequency region from 0.01 to  $10^5 \text{ Hz}$  with alternating current (AC) voltage of 5 mV. Transient photocurrent responses measurements were performed by a 300 W xenon lamp (Newport, model 69911, USA) coupled with an AM 1.5 G filter. Preparation of COF film for electrochemical tests: 10 mg of COF sample was dissolved in a mixed solution of 1.5 mL isopropanol and 10  $\mu\text{L}$  Nafion, and then sonicated for 3 h to form the homogeneous suspension. The obtained suspension was spin-coated on F-doped  $\text{SnO}_2$ -coated glass (FTO glass, the effective working area of  $1 \text{ cm}^2$ ).

### 2.5. Electron paramagnetic resonance (EPR) measurements

Hydroxyl radical detection: 5,5-dimethyl-1-pyrroline-N-oxide (DMPO) was selected as the trapping agent during the measurements. 5 mL of the aqueous solution with the 5 mg COF sample was mixed with 100  $\mu\text{L}$  of DMPO trapping agent solution (10 mM). After being irradiated for 300 s with visible light, the mixed solution was characterized by an electron spin resonance spectrometer. Superoxide radical detection: 5 mL of the methanol solution with the 5 mg COF sample was mixed with 100  $\mu\text{L}$  of DMPO trapping agent solution (10 mM). After being irradiated for 300 s with visible light, then the mixed solution was detected.

### 2.6. Detailed measurements

More experimental details are described in [Supporting Information](#),

including chemicals and reagents, characterizations, solar-to-chemical conversion (SCC) efficiency calculations, and computational method, etc.

### 3. Results and discussion

#### 3.1. Structural characterizations of COF photocatalyst

A thioether-decorated triazine-based COF (TDB-COF) was constructed and prepared based on a multicomponent strategy by an imine condensation of the monomers (Fig. 1 and Scheme S1). Specifically, in this multiple-component [1 + 2] condensation system, the hexagonal TDB-COF was precisely synthesized by using one knot (TFPT) and two linker units (DETH and BETH) under solvothermal conditions, while the molar ratio of two linkers between DETH and BETH is 1:2. Subsequently, the resultant TDB-COF was chosen as the sole photocatalyst for overall  $\text{H}_2\text{O}_2$  photosynthesis without any sacrificial agents or cocatalysts.

The synthesized photocatalyst was determined by a series of elaborate characterizations. Fourier transform infrared (FT-IR) spectra was performed to investigate the characteristic functional groups of COF photocatalyst. Compared with the FT-IR of the monomers, TDB-COF not only reveals a disappearance of stretching peak for aldehyde group ( $1700\text{ cm}^{-1}$ ) of TFPT but also shows a presence of the hydrazone bond at  $1618\text{ cm}^{-1}$  (Fig. 2a), indicating a formation of hydrazone linkage [32]. Meanwhile, strong stretching bands of TDB-COF at  $1510$  and  $812\text{ cm}^{-1}$  can be attributed to the existence of the triazine ring [33,34]. The chemical structure of TDB-COF was further investigated by solid-state  $^{13}\text{C}$  CP-MAS nuclear magnetic resonance (NMR) spectrum (Fig. S1).

The characteristic peaks at 160 and 150 ppm can be attributed to the carbon atoms of the  $\text{C}=\text{O}$  and hydrazone bonds respectively, while the signal at 169 ppm means the existence of the triazine ring. The signals between 66 and 14 ppm correspond to the thioether groups and ethoxy groups of TDB-COF. Besides, elemental analysis (EA) results of C, H, N and S for TDB-COF match well with the theoretical values (Table S1). The crystallinity of TDB-COF was evaluated by measuring powder X-ray diffraction (PXRD). Compared to the monomers, the experimental PXRD pattern of TDB-COF shows a strongly predominant peak at  $3.1^\circ$  corresponded to the (100) plane (Fig. S2), indicating an excellent crystallinity. The high crystallinity of TDB-COF can be beneficial for the photogenerated charge transport [35]. The stacking model of TDB-COF was determined by the theoretical simulation using Materials Studio 7.0 (Fig. S3 and Fig. S4). The simulated AA eclipsed stacking model of TDB-COF is in agreement with the experimental PXRD pattern (Fig. 2b). By contrast, the simulated PXRD pattern for the AB staggered structure cannot correspond well to the experimental PXRD pattern.

The Brunauer-Emmett-Teller (BET) surface area and pore volume of TDB-COF were investigated by nitrogen adsorption-desorption isotherm measurement at 77 K. The  $\text{N}_2$  sorption measurement of TDB-COF shows a typical type IV adsorption isotherm and reveals the formation of mesopores (Fig. 2c). The BET surface area and pore volume of TDB-COF are  $243.2\text{ m}^2\text{ g}^{-1}$  and  $0.16\text{ cm}^3\text{ g}^{-1}$ , respectively. Furthermore, the pore width distribution of TDB-COF is estimated to be 3.2 nm (the inset in Fig. 2c). The morphology and structure size of TDB-COF were determined by scanning electron microscopy (SEM) and transmission electron microscopy (TEM). TDB-COF exhibits uniform nano-strips with an average size of nearly 180 nm in diameter (Fig. 2d and

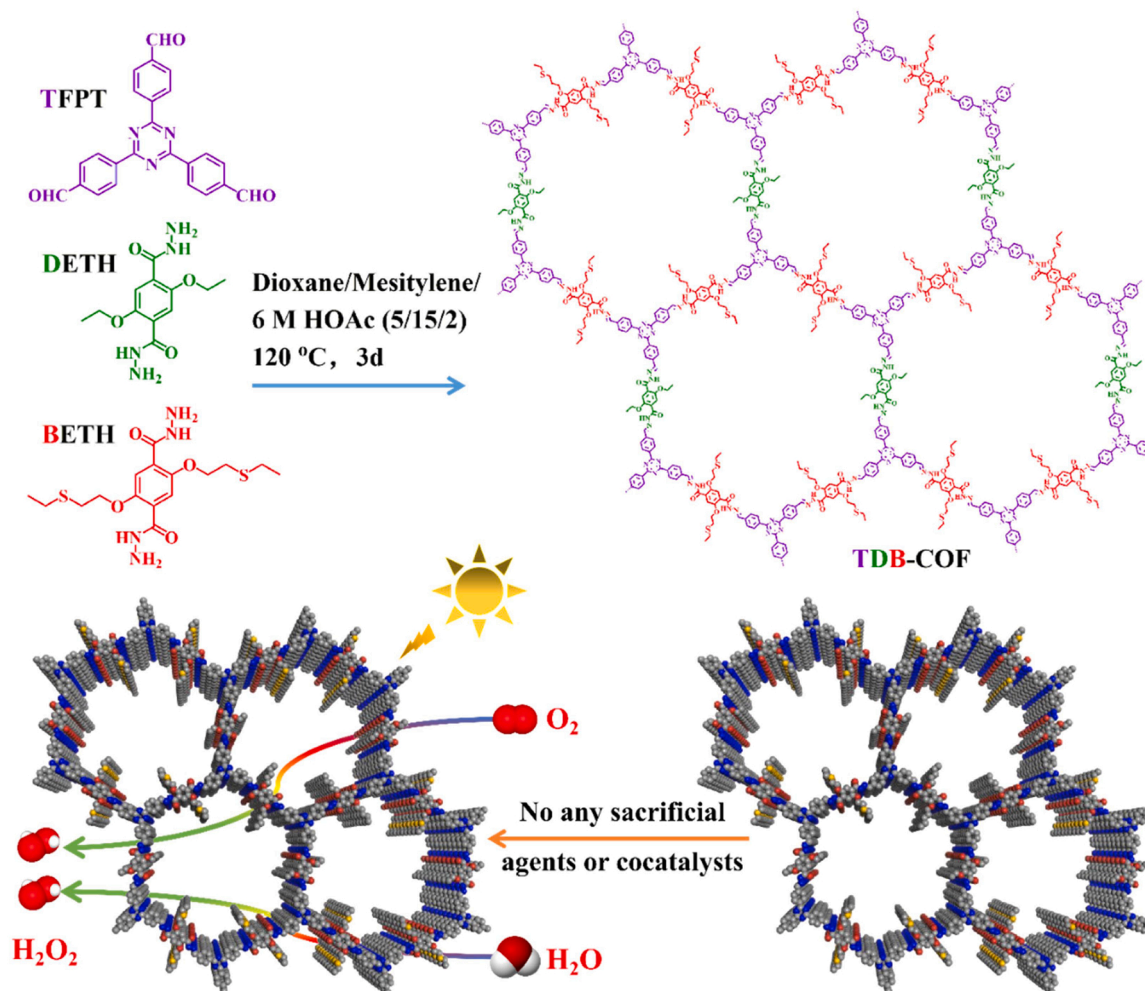
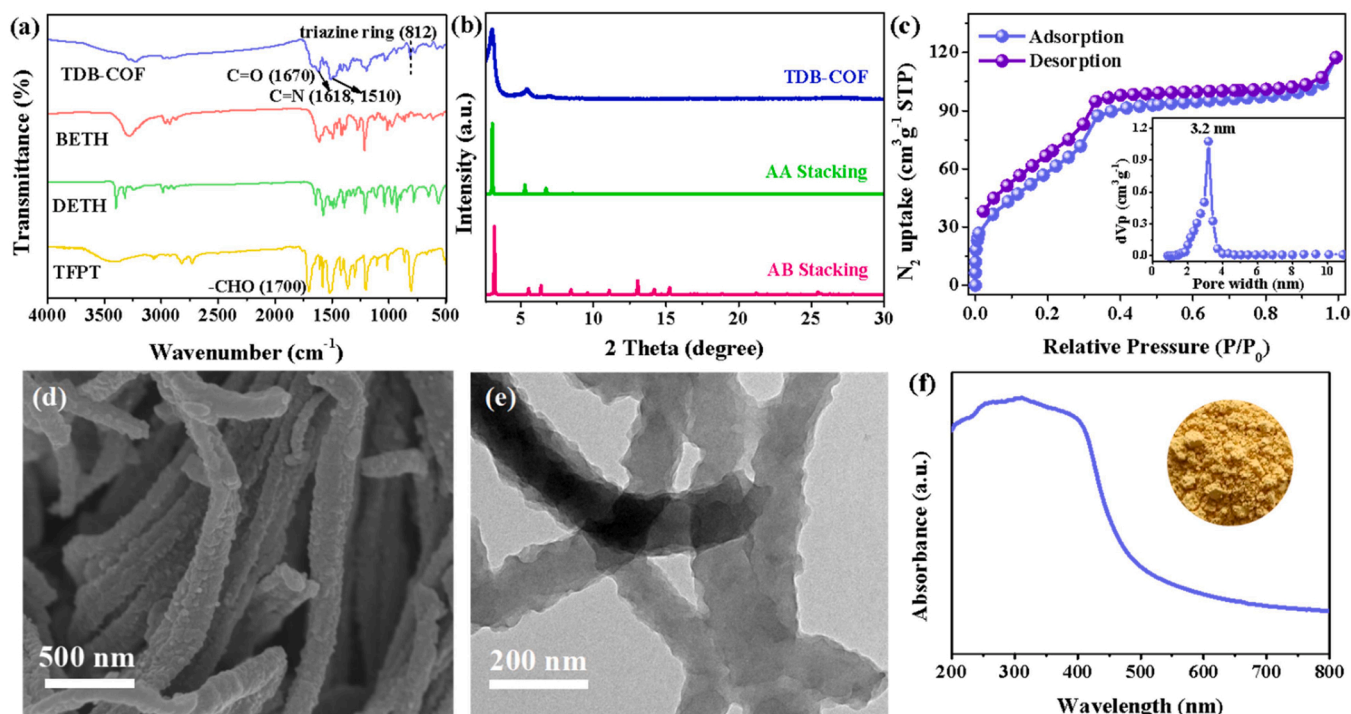


Fig. 1. Schematic representation of the preparation of TDB-COF based on a multicomponent strategy and its application for overall photocatalytic  $\text{H}_2\text{O}_2$  production.





**Fig. 2.** (a) FT-IR spectra for TFPT, DETH, BETH, and TDB-COF, (b) PXRD patterns of experimental and simulated TDB-COF, (c) Nitrogen adsorption–desorption isotherm and pore width distribution of TDB-COF, (d) SEM and (e) TEM images of TDB-COF, (f) UV–vis DRS of TDB-COF, the inset is optical image of TDB-COF photocatalyst.

**Fig. S5).** The TEM result further confirms that TDB-COF is constructed by lots of homogeneous nanostrips (Fig. 2e and Fig. S6). X-ray photoelectron spectroscopy (XPS) was measured to investigate the elemental composition and valence state of TDB-COF. XPS spectra of TDB-COF (Fig. S7) exhibits the characteristic peaks of the elements C, N, O, and S. As Fig. S8 displayed, the C 1s spectra of TDB-COF shows that the triple peaks at 284.8, 286.4 and 288.0 eV can be attributed to the interaction between C and C atoms,  $sp^2$ -bonded carbon, and C=O bonds [36], respectively. And the signal at 290.8 eV corresponds to the characteristic shake up line of the aromatic carbon. In addition, the N 1s spectra of TDB-COF indicates that the strongly characteristic peak is assigned to the N–N bonds, while the signal at 398.6 eV is present at  $sp^2$ -hybridized aromatic nitrogen bonded to carbon atoms (C=N–C) [37, 38]. The double peaks at 533.2 and 531.4 eV in O 1s XPS of TDB-COF can be attributed to the C=O and C–O bonds, respectively. The characteristic peaks in S 2p XPS of TDB-COF confirm the presence of thioether groups, which is consistent with the solid-state  $^{13}C$  NMR result. Thermogravimetric analysis (TGA) shows that TDB-COF possesses thermal stability up to around 258 °C under argon atmosphere (Fig. S9). Ultraviolet–visible diffuse-reflectance spectra (UV–vis DRS) was performed to investigate the optical property of TDB-COF. UV–vis DRS of TDB-COF shows that it has a wide absorption range up to 550 nm in the visible light region, corresponding to the bright yellow powder and revealing a strong light absorption capacity (Fig. 2f).

### 3.2. Photocatalytic $H_2O_2$ production performance

The photocatalytic  $H_2O_2$  production experiments of TDB-COF photocatalyst can be evaluated from the amount of  $H_2O_2$  detected by UV–vis spectroscopy and choose potassium titanium oxalate as peroxide indicator. As shown in Fig. S10, the fitted curve of UV–vis absorbance versus different  $H_2O_2$  concentration was provided. The hydrophilicity of TDB-COF was studied by the water contact angle (CA) measurement (Fig. S11). The surface of TDB-COF exhibits a hydrophilic capacity with a water CA of 56.1°. The photocatalytic performance test was performed by using 10 mL pure water with 10 mg COF sample under visible light

irradiation without any sacrificial agents or cocatalysts. TDB-COF can achieve steady photocatalytic  $H_2O_2$  production with a rate of 231  $\mu\text{mol g}^{-1} \text{h}^{-1}$  under the air atmosphere (Fig. 3a). Surprisingly, the photocatalytic  $H_2O_2$  production of TDB-COF can reach up to 723.5  $\mu\text{mol g}^{-1} \text{h}^{-1}$  in the  $O_2$  saturated system, which is competitive with some COFs and other inorganic photocatalysts reported previously [25,39–44] (Fig. 3b, more details in Table S2). Furthermore, TDB-COF exhibits strong cyclic stability for four cycles under  $O_2$  or air atmosphere condition (Fig. 3c), indicating that TDB-COF can serve as a stable metal-free photocatalyst for efficient photocatalytic  $H_2O_2$  production. The apparent quantum yield (AQY) was measured by using different band-pass filters with single wavelength at 365, 400, 550, and 650 nm, respectively (Fig. S12 and Table S3). The AQY values of TDB-COF are 1.4% and 1.0% at the wavelength of 365 and 400 nm, respectively. And its solar-to-chemical conversion (SCC) efficiency can be up to 0.39% (see more details in Supporting Information). Noticeably, the photocatalytic  $H_2O_2$  production of TDB-COF can increase to 1000.1  $\mu\text{mol g}^{-1} \text{h}^{-1}$  by adding 10% ethanol as sacrificial agent (Fig. S13). These above results indicate that TDB-COF shows a remarkable capacity for  $H_2O_2$  photosynthesis with or without any sacrificial agents. To verify whether protons are favorable for the coupled electron transfer, we studied the relationship between the photocatalytic activity and the different proton concentration of solution (Fig. 3d). The concentration of protons of the photocatalytic system was regulated by using phosphate buffer solution (PBS) to control the pH values (1.0, 3.0, 5.0, 7.0, and 9.0) of the solution. From the values of pH 1–3, the photocatalytic activity of TDB-COF is positively affected by the concentration of protons, which indicates that the protons conduction can be facilitated by the ordered pore distribution of TDB-COF framework and a higher proton conductivity is beneficial for photocatalytic  $H_2O_2$  production [11]. However, after the proton concentration reached a certain level (pH  $\geq$  5), the photocatalytic  $H_2O_2$  production of TDB-COF is decreased and slowly affected by the pH values.

In order to study the influence of thioether groups modification for photocatalytic  $H_2O_2$  production performance, TFPT-COF without any thioether groups was further synthesized under the same conditions

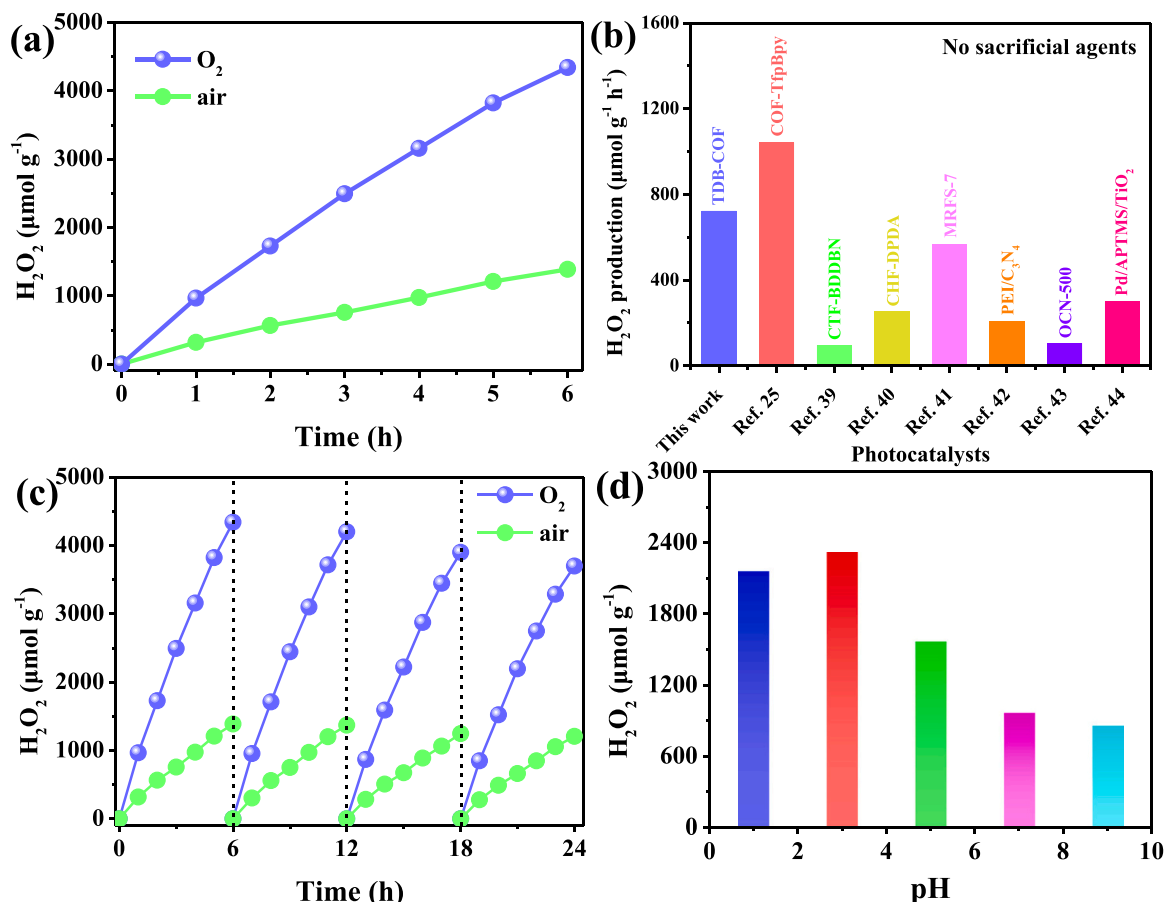


**Fig. 3.** (a) Photocatalytic  $\text{H}_2\text{O}_2$  production of TDB-COF, (b) The photocatalytic performance of TDB-COF compared with other representative photocatalysts, (c) Cycling stability of  $\text{H}_2\text{O}_2$  generation of TDB-COF without any sacrificial agents or cocatalysts, (d) Relationship between the values of pH in the reaction solution and the photocatalytic  $\text{H}_2\text{O}_2$  production of TDB-COF.

(Fig. S14 and Fig. S15), which is an analogue of thioether-containing TDB-COF. As Fig. S16 displayed, TFPT-COF can achieve a photocatalytic  $\text{H}_2\text{O}_2$  generation rate of  $79.2 \mu\text{mol g}^{-1} \text{h}^{-1}$  without any sacrificial agents under the same photocatalytic conditions, which is lower than that of thioether-containing TDB-COF ( $723.5 \mu\text{mol g}^{-1} \text{h}^{-1}$ ). This result indicates that the introduction of thioether groups into the structure of COFs can be beneficial for enhanced photocatalytic  $\text{H}_2\text{O}_2$  generation. To better understand the related charge transport progresses and visible light responses between TDB-COF and TFPT-COF, electrochemical impedance spectroscopy (EIS) of the photocatalysts and the transient photocurrent responses under light illumination were further measured. The EIS curves can be fitted to an equivalent circuit diagram by using Z-view software (inset in Fig. 4a), where  $R_s$ ,  $R_{ct}$  and CPE represent the resistance of the electrolyte, charge transfer resistance at the photocatalyst/electrolyte interface, and capacitance phase element, respectively. Compared with TFPT-COF, TDB-COF shows a lower semicircular diameter of Nyquist curve and also reveals a smaller interfacial charge transport resistance (Fig. 4a and Table S4), indicating that the modification of thioether groups can effectively accelerate the interfacial charge transport kinetics [45]. As shown in Fig. 4b, TDB-COF has a higher photocurrent density than that of TFPT-COF, which confirms that the introduction of thioether groups boosts up the generation of more photoexcited charges and promotes the photogenerated electrons-holes separation [46]. Furthermore, photoluminescence (PL) and time-resolved photoluminescence (TRPL) spectra were performed to investigate the photogenerated carriers behavior. The PL intensity of TDB-COF is slightly quenched in comparison with TFPT-COF (Fig. 4c), meaning a suppressed recombination of the photogenerated electrons and holes [47]. As Fig. 4d displayed, the average lifetime of TDB-COF

(20.02 ns) is lower than that of TFPT-COF (23.45 ns), suggesting that the photogenerated carriers separation and transport of TDB-COF is faster, which is advantageous to drive photocatalytic redox reactions [39,48–50]. These above results demonstrate that the modification of thioether groups can not only accelerate the interfacial charge transport kinetics but also promote the photogenerated carriers separation, thus ultimately enhancing the photocatalytic performance of TDB-COF.

### 3.3. Investigation on the recovery of TDB-COF photocatalyst

To investigate the structural changes of photocatalyst, the TDB-COF recovered from the cyclic experiment was further studied by a series of structural characterizations. As PXRD pattern displayed (Fig. S17), the recycled TDB-COF loses its long-range order because of the exfoliation of the layered COF in aqueous solution [51], while its crystallinity inevitably decreases after continuous photocatalytic reaction. From the PXRD of the recycled TDB-COF, no characteristic peaks of the monomers (TFPT, DETH, and BETH) can be found, indicating that its structure does not decompose. It is worth mentioning that the chemical linkages and characteristic functional groups of TDB-COF can be intact before and after photocatalytic cycling stability test (Fig. 5a), suggesting a chemical structure stability. As shown in Fig. 5b–d, the characteristic peaks of C 1 s, N 1 s, and O 1 s of TDB-COF show no obvious peak shifts after the photocatalytic reaction, further indicating a framework integrity without decomposition. At the same time, the characteristic peaks in S 2p of TDB-COF upshift from 163.2 eV to 165.9 eV and a weak signal is generated at 163.4 eV (Fig. 5e), which indicates that the thioether groups of TDB-COF are oxidized and generated into sulfoxides during the photocatalytic process. TDB-COF shows homogeneous nanostrips in

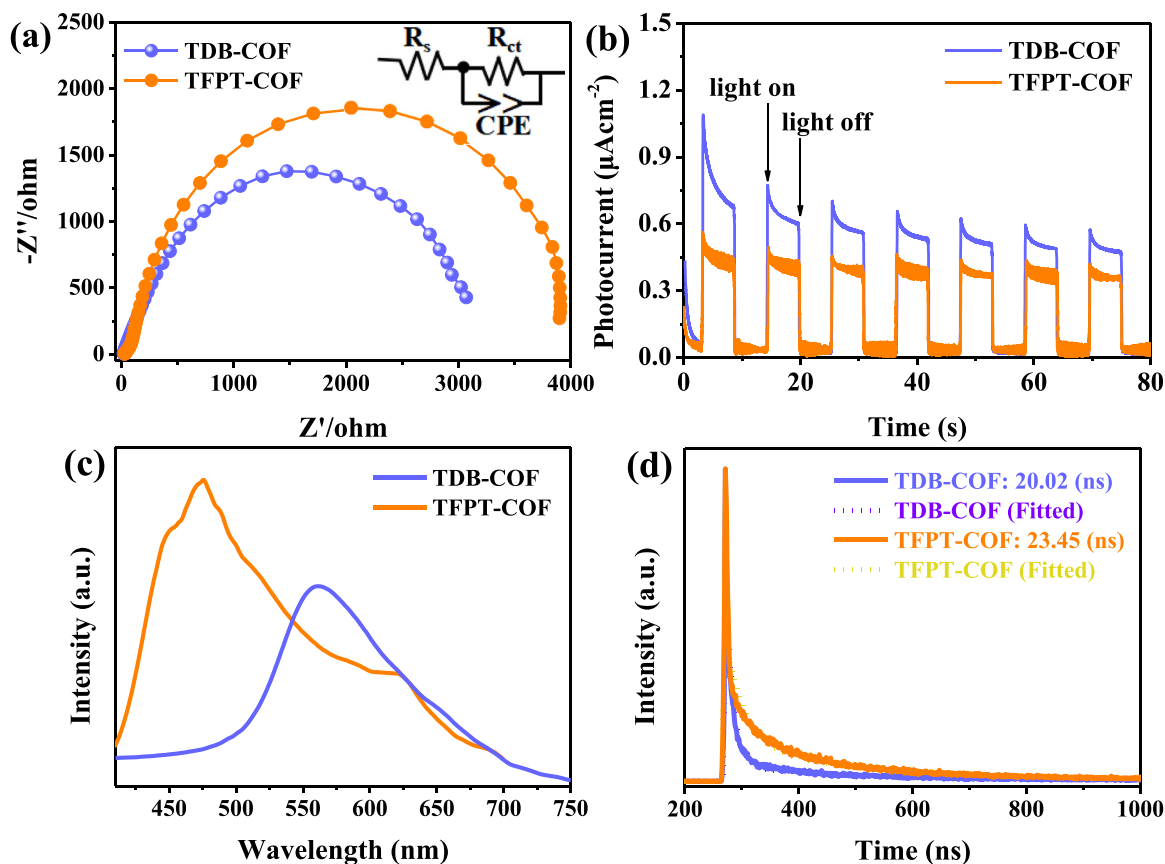


Fig. 4. (a) EIS Nyquist curves of TDB-COF and TFPT-COF, the inset is equivalent circuit diagram, (b) Transient photocurrent responses of TDB-COF and TFPT-COF under light illumination, (c) Photoluminescence (PL) emission spectra of TDB-COF and TFPT-COF in the solid-state, (d) Time-resolved Photoluminescence (TRPL) spectra of TDB-COF and TFPT-COF.

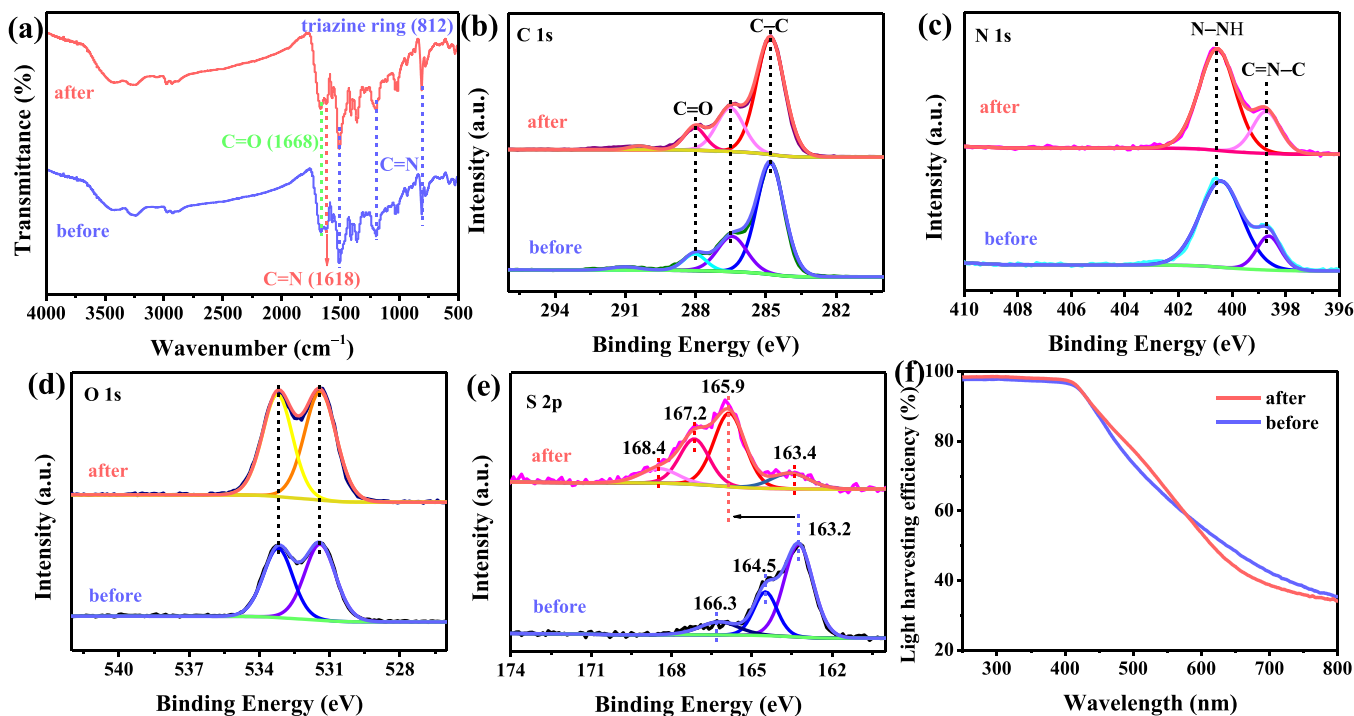


Fig. 5. (a) FT-IR spectra of TDB-COF obtained before and after photocatalytic cycles, XPS spectra of (b) C 1s, (c) N 1s, (d) O 1s, and (e) S 2p for TDB-COF obtained before and after photocatalytic cycles, (f) Light harvesting efficiency of TDB-COF obtained before and after photocatalytic cycles.

morphology and its structure size becomes rougher with an average size of 320 nm in width dimension after photocatalytic cycling reaction (Fig. S18). And the nanoparticles scattered on the surface of TDB-COF become more visible, which is beneficial for the light harvesting. Ultimately, the recycled TDB-COF still maintains good visible light absorption ability (Fig. S19), meaning a retained photoactivity. Light harvesting efficiency (LHE) of TDB-COF can be calculated from the absorbance of UV-vis DRS based on the formula ( $LHE = 1 - 10^{-A(\lambda)}$ , A represents absorbance) [52]. Clearly, TDB-COF retains high light capture efficiency in the visible light region (Fig. 5f), indicating its remarkable photostability.

### 3.4. Photocatalytic working mechanism

To clarify the photocatalytic route of  $H_2O_2$  generation for TDB-COF, a series of contrast experiments were conducted. As Fig. 6a displayed, the photocatalytic performance of TDB-COF was tested under different atmospheric conditions (Ar/Air/ $O_2$ ). Before the photocatalytic experiments, the testing systems with 10 mg photocatalyst and 10 mL  $H_2O$  were saturated with Ar, air or  $O_2$  for 30 min, respectively. Under the Ar saturated system, the photocatalytic  $H_2O_2$  production with a yield of  $23.5 \mu\text{mol g}^{-1} \text{h}^{-1}$  was achieved with TDB-COF as photocatalyst, which demonstrates the existence of WOR process. Besides, the photocatalytic  $H_2O_2$  generation ( $723.5 \mu\text{mol g}^{-1} \text{h}^{-1}$ ) over TDB-COF under the  $O_2$  saturated system shows a remarkable increase compared with that under air ( $231.0 \mu\text{mol g}^{-1} \text{h}^{-1}$ ) or Ar condition. Obviously, with the increase of oxygen concentration, the  $H_2O_2$  production rate by TDB-COF increases significantly, which confirms that  $H_2O_2$  can be produced by oxygen reduction and ORR plays a dominant role in this photocatalytic system.

Quenching experiments of the active species for TDB-COF were performed to further understand the pathway of photocatalytic  $H_2O_2$  production (Fig. 6b). When electron and  $\cdot O_2^-$  are quenched, the  $H_2O_2$  yield of TDB-COF decreases sharply and only a little  $H_2O_2$  production can be detected, indicating that ORR plays a significantly decisive role in this photocatalytic system [53]. To determine the active oxygen species during the photocatalytic process, electron paramagnetic resonance (EPR) spectra was measured by using DMPO as spin-trap agent (Fig. 6c). The typical characteristic peaks of DMPO- $O_2^-$  for TDB-COF can be clearly observed under visible light irradiation, suggesting the production of  $\cdot OOH$  intermediate species [29]. This result further indicates that ORR is a  $2e^-$  two-steps oxygen reduction route to produce  $H_2O_2$  ( $O_2 \rightarrow \cdot O_2^- \rightarrow H_2O_2$ ) in this photocatalytic system. Meanwhile, the signals of DMPO- $OH\cdot$  for TDB-COF are easily detected (Fig. 6d), which confirms that WOR route is a  $2e^-$  two-steps process with  $OH\cdot$  as the intermediate species. Specifically, the photocatalytic water oxidation process by TDB-COF is to release  $OH\cdot$  firstly, and then two  $OH\cdot$  coupled to generate  $H_2O_2$  ( $H_2O \rightarrow OH\cdot \rightarrow H_2O_2$ ). Furthermore, the rotating disk electrode (RDE) measurement result (Fig. S20) further confirms that the average electron transfer number of ORR is nearly 2 on TDB-COF, which is consistent with the EPR result. The process of  $H_2O_2$  photosynthesis by TDB-COF is a dominant  $2e^-$  two-steps ORR combining with a  $2e^-$  two-steps WOR.

To further investigate the working mechanism of photocatalytic  $H_2O_2$  generation, it is significantly crucial to determine the energy band structure of COFs. As shown in Fig. 7a, compared with TFPT-COF without any thioether groups, the thioether-decorated TDB-COF has a wider visible light absorption range, which indicates a stronger visible light harvesting capacity and corresponds to the enhanced

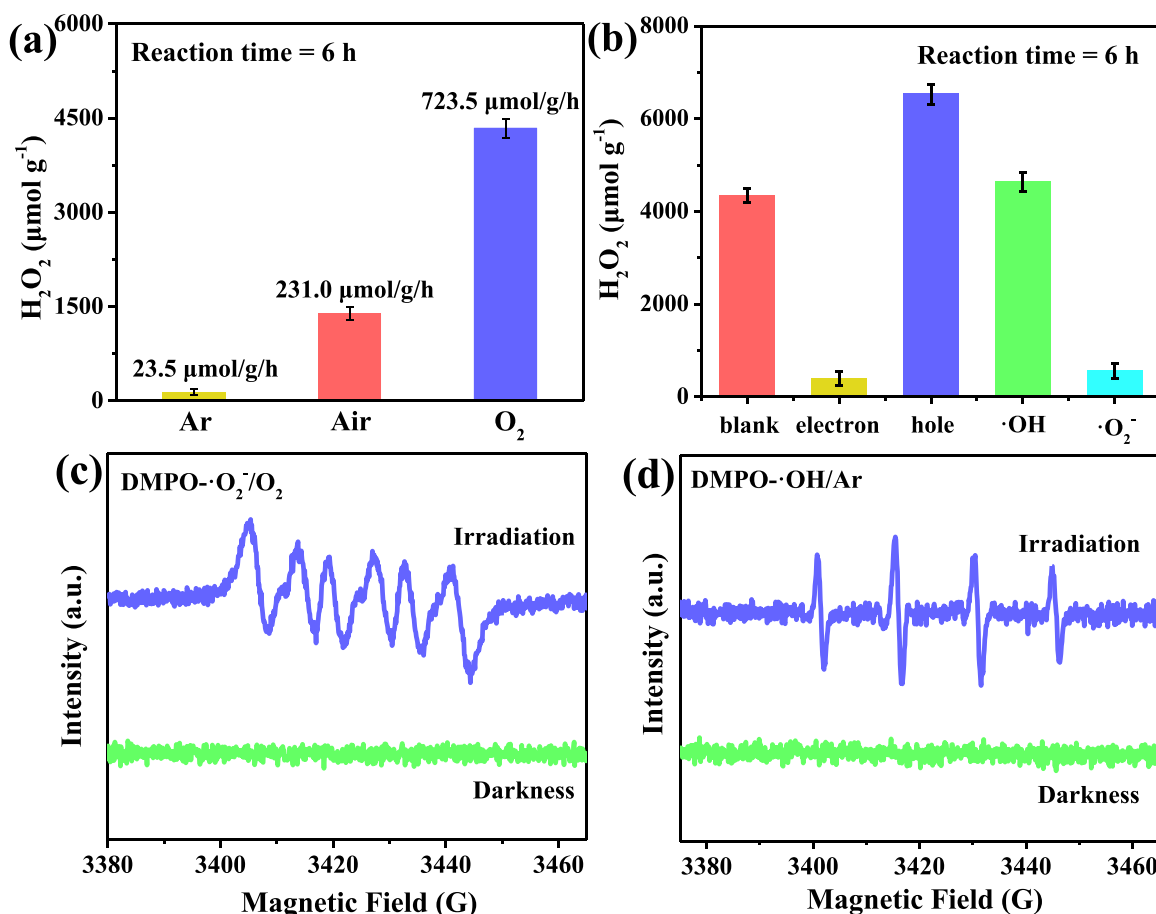


Fig. 6. (a) The comparison of the photocatalytic  $H_2O_2$  production for TDB-COF at different atmospheres (Ar/Air/ $O_2$ ) under visible light, (b) The contribution of different active species to photocatalytic  $H_2O_2$  production of TDB-COF, (c) DMPO spin-trapping EPR spectra of TDB-COF for measuring  $\cdot O_2^-$ , (d) DMPO spin-trapping EPR spectra of TDB-COF for measuring  $OH\cdot$  under visible light and dark conditions.



photocatalytic  $\text{H}_2\text{O}_2$  production performance. Meanwhile, the band gap of TDB-COF and TFPT-COF can be calculated to be 2.67 eV and 2.82 eV by using a Tauc-plot method (Fig. 7b), respectively. These results confirm that the modification of thioether groups can not only broaden the visible light absorption of COFs but also narrow the optical band gap, which is advantaged to the  $\text{H}_2\text{O}_2$  photosynthesis. According to the VB-XPS spectra (Fig. S21), the valence band (VB) values of TDB-COF and TFPT-COF are speculated to be 1.80 and 1.43 eV, respectively. Combining the band gap with the VB results, the conduction band (CB) values of TDB-COF and TFPT-COF are further calculated to be  $-0.87$  and  $-1.39$  eV vs. NHE, respectively. Therefore, the energy band structures of TDB-COF and TFPT-COF are illustrated in Fig. 7c. Obviously, the redox potential of TDB-COF can not only generate  $\text{H}_2\text{O}_2$  from ORR but also meet the theoretical conditions for WOR to produce  $\text{H}_2\text{O}_2$ . These results indicate that the introduction of functionalized thioether groups can legitimately regulate the energy band structure of TDB-COF for enhanced photocatalytic  $\text{H}_2\text{O}_2$  production. Based on the above comprehensive investigations, the working mechanism of photocatalytic  $\text{H}_2\text{O}_2$  production over TDB-COF is proposed as shown in Fig. 7d. TDB-COF photocatalyst exhibits excellent visible light absorption, suitable band gap, and strong photostability. Under visible light irradiation, TDB-COF undergoes photoexcitation to generate photogenerated electrons, which transfer to the CB of TDB-COF and further participate in a  $2e^-$  two-steps ORR to generate  $\text{H}_2\text{O}_2$ . Subsequently, the photogenerated holes accumulated on the VB of TDB-COF photocatalyst participate in a  $2e^-$  two-steps WOR to produce  $\text{H}_2\text{O}_2$ .

Experimental results conclusively confirm that the introduction of thioether groups is crucial for enhanced photocatalytic  $\text{H}_2\text{O}_2$  production. Density functional theory calculation was then carried out to provide more insights into the photocatalytic process of TDB-COF. In the  $2e^-$  WOR pathway, the formation of  $\text{OH}^*$  is an intermediate state of

WOR process, which is crucial for the formation of  $\text{H}_2\text{O}_2$  by WOR. When the thioether groups of TDB-COF and ethoxy groups of TFPT-COF are respectively used as the active sites (Fig. 8a and b), the Gibbs free energy change ( $\Delta G$ ) of the  $\text{OH}^*$  intermediate for TDB-COF below TFPT-COF (Fig. 8c), which is beneficial for generating  $\text{H}_2\text{O}_2$  through a  $2e^-$  two-steps WOR. And the detection of  $\text{OH}^\bullet$  during the previous EPR measurement process and contrast experiments under different atmospheric conditions (Ar/Air/ $\text{O}_2$ ) can further confirm the formation of  $\text{OH}^\bullet$  and  $\text{H}_2\text{O}_2$ . For the  $2e^-$  ORR pathway, the  $\text{O}_2$  adsorption on COFs is the most critical step to reduce  $\text{O}_2$  into  $\text{H}_2\text{O}_2$ . Triazine group is a kind of typical electron acceptor, which can combine with electron donor to establish a photogenerated electron transfer platform. When triazine group is used as the  $\text{O}_2$  adsorption sites of TDB-COF and TFPT-COF respectively, calculation results show that the endoperoxide species of TDB-COF have a significantly lower Gibbs free energy than that of TFPT-COF (Fig. 8d). Therefore, introducing thioether groups into TDB-COF can effectively promote the  $\text{O}_2$  adsorption and subsequent  $\text{H}_2\text{O}_2$  formation through an important  $2e^-$  ORR pathway. Ultimately, based on the above experimental and computational results, we have a clear understanding of photocatalytic pathways toward  $\text{H}_2\text{O}_2$  production over TDB-COF. The overall  $\text{H}_2\text{O}_2$  photosynthesis of TDB-COF is a dominant  $2e^-$  two-steps ORR process combining with a  $2e^-$  two-steps WOR.

#### 4. Conclusion

In summary, a novel thioether-functionalized triazine-based COF (TDB-COF) was designed and synthesized via a multicomponent strategy towards efficient overall  $\text{H}_2\text{O}_2$  photosynthesis from  $\text{H}_2\text{O}$  and  $\text{O}_2$ . TDB-COF possesses the remarkable light absorption, ordered thioether groups, and suitable band structure for photocatalytic  $\text{H}_2\text{O}_2$  production. TDB-COF can achieve good photocatalytic activity with a  $\text{H}_2\text{O}_2$

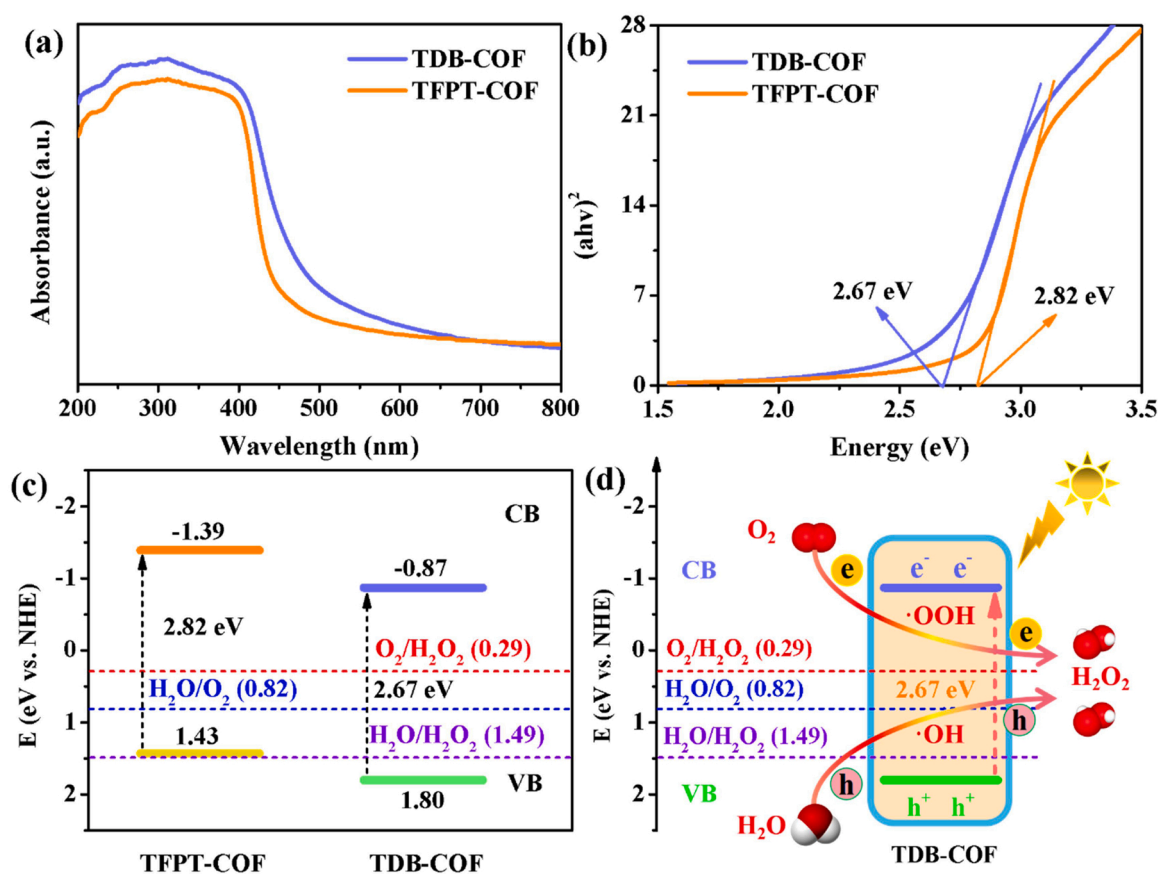
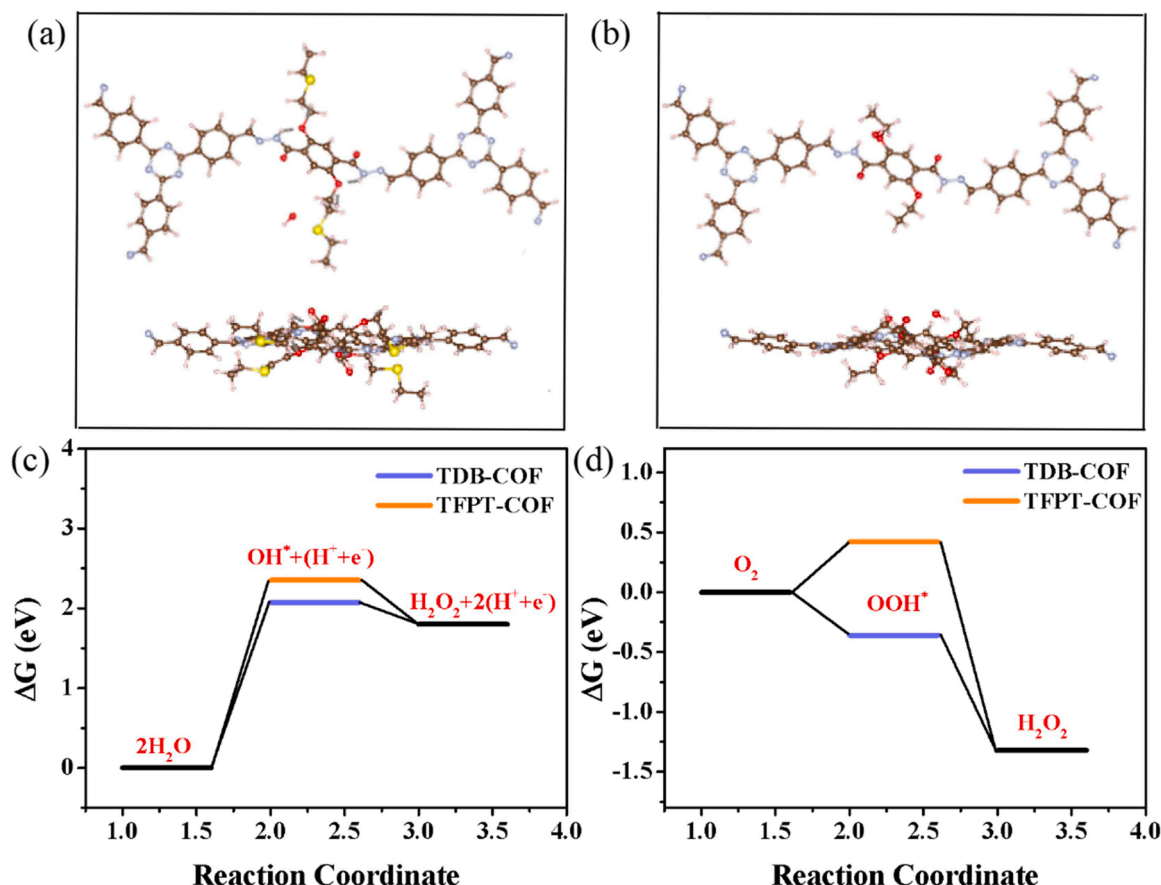


Fig. 7. (a) UV-Vis DRS and (b) band gap of TDB-COF and TFPT-COF, (c) The energy band structure of TDB-COF and TFPT-COF, (d) The overall  $\text{H}_2\text{O}_2$  photosynthesis over TDB-COF.





**Fig. 8.** (a) Thioether linker as active site in TDB-COF (C: grey, N: blue, O: red, S: yellow), (b) Ethoxy linker as active site in TFPT-COF (top view and side view), Gibbs free energy diagrams of (c) 2e<sup>-</sup> two-steps WOR pathway and (d) 2e<sup>-</sup> two-steps ORR pathway toward H<sub>2</sub>O<sub>2</sub> production on TDB-COF and TFPT-COF.

production rate of 723.5  $\mu\text{mol g}^{-1} \text{h}^{-1}$  without any sacrificial agents or cocatalysts and maintain remarkable cyclic stability. The AQY value of TDB-COF is 1.4% at 365 nm, while its SCC efficiency is 0.39% under the simulated AM 1.5 G illumination. Besides, TDB-COF also maintains its chemical structure stability after photocatalytic cycling tests. The introduction of thioether groups can effectively broaden the visible-light absorption of TDB-COF and regulate its band structure suitable for 2e<sup>-</sup> two-steps WOR to generate H<sub>2</sub>O<sub>2</sub> and accelerate a 2e<sup>-</sup> two-steps ORR process, thus ultimately promoting overall H<sub>2</sub>O<sub>2</sub> photosynthesis. This work not only confirms the feasibility of the thioether-containing COFs towards efficient overall photocatalytic H<sub>2</sub>O<sub>2</sub> production, but also provides valuable suggestions for the design and development of COFs towards chemical fuels photosynthesis.

#### CRediT authorship contribution statement

**Zhiming Zhou:** Investigation, Data curation, Writing – original draft, Revision and Proof. **Minghui Sun:** Data curation. **Yanbin Zhu:** Data curation. **Peize Li:** Data curation. **Yanrong Zhang:** Review and editing. **Mingkui Wang:** Conceptualization. **Yan Shen:** Writing – review & editing, Funding acquisition, Project administration, Revision & Proof.

#### Declaration of Competing Interest

The authors declare that they have no known competing financial interests or personal relationships that could have appeared to influence the work reported in this paper. All authors have agreed to submit the manuscript to your journal, and this work has not been submitted elsewhere for publication, in whole or in part nor is it being considered for publication elsewhere. No conflict of interest exists in the submission

of this manuscript, and manuscript is approved by all authors.

#### Data Availability

Data will be made available on request.

#### Acknowledgements

This work was financially supported from the NSFC Major International (Regional) Joint Research Project NSFC-SNSF (51661135023), the National Natural Science Foundation of China (21673091), the Fundamental Research Funds for the Central Universities (HUST: 2016YXMS031), the Director Fund of the WNLO, and the Open Funds of the State Key Laboratory of Electroanalytical Chemistry (SKLEAC201607). The authors also thank the Analytical and Testing Center of HUST and the facility support of the Center for Nanoscale Characterization & Devices (CNCD), Wuhan National Laboratory for Optoelectronics (WNLO) of Huazhong University of Science and Technology (HUST) for the samples characterization.

#### Appendix A. Supporting information

Supplementary data associated with this article can be found in the online version at doi:10.1016/j.apcatb.2023.122862.

#### References

- [1] Y. Bu, Y. Wang, G.F. Han, Y. Zhao, X. Ge, F. Li, Z. Zhang, Q. Zhong, J.B. Baek, Carbon-based electrocatalysts for efficient hydrogen peroxide production, *Adv. Mater.* 33 (2021) 2103266.

- [2] Y. Isaka, Y. Kawase, Y. Kuwahara, K. Mori, H. Yamashita, Two-phase system utilizing hydrophobic metal-organic frameworks (MOFs) for photocatalytic synthesis of hydrogen peroxide, *Angew. Chem. Int. Ed.* 58 (2019) 5402–5406.
- [3] M. Gu, Y. Yang, L. Zhang, B. Zhu, G. Liang, J. Yu, Efficient sacrificial-agent-free solar H<sub>2</sub>O<sub>2</sub> production over all-inorganic S-scheme composites, *Appl. Catal. B: Environ.* 324 (2023), 122227.
- [4] M. Sun, X. Wang, Y. Li, H. Pan, M. Murugananthan, Y. Han, J. Wu, M. Zhang, Y. Zhang, Z. Kang, Bifunctional Pd-Ox center at the liquid-solid-gas triphase interface for H<sub>2</sub>O<sub>2</sub> photosynthesis, *ACS Catal.* 12 (2022) 2138–2149.
- [5] S. Li, G. Dong, R. Hailili, L. Yang, Y. Li, F. Wang, Y. Zeng, C. Wang, Effective photocatalytic H<sub>2</sub>O<sub>2</sub> production under visible light irradiation at g-C<sub>3</sub>N<sub>4</sub> modulated by carbon vacancies, *Appl. Catal. B: Environ.* 190 (2016) 26–35.
- [6] Y. Sun, L. Han, P. Strasser, A comparative perspective of electrochemical and photochemical approaches for catalytic H<sub>2</sub>O<sub>2</sub> production, *Chem. Soc. Rev.* 49 (2020) 6605–6631.
- [7] S. Wu, H. Yu, S. Chen, X. Quan, Enhanced photocatalytic H<sub>2</sub>O<sub>2</sub> production over carbon nitride by doping and defect engineering, *ACS Catal.* 10 (2020) 14380–14389.
- [8] Y. Kofuji, Y. Isobe, Y. Shiraiishi, H. Sakamoto, S. Tanaka, S. Ichikawa, T. Hirai, Carbon nitride-aromatic diimide-graphene nanohybrids: metal-free photocatalysts for solar-to-hydrogen peroxide energy conversion with 0.2% efficiency, *J. Am. Chem. Soc.* 138 (2016) 10019–10025.
- [9] Z. Zhu, H. Pan, M. Murugananthan, J. Gong, Y. Zhang, Visible light-driven photocatalytically active g-C<sub>3</sub>N<sub>4</sub> material for enhanced generation of H<sub>2</sub>O<sub>2</sub>, *Appl. Catal. B: Environ.* 232 (2018) 19–25.
- [10] H.L. Hou, X.K. Zeng, X.W. Zhang, Production of hydrogen peroxide by photocatalytic processes, *Angew. Chem. Int. Ed.* 59 (2020) 17356–17376.
- [11] Q. Wu, Y. Liu, J. Cao, Y. Sun, F. Liao, Y. Liu, H. Huang, M. Shao, Z. Kang, A function-switchable metal-free photocatalyst for the efficient and selective production of hydrogen and hydrogen peroxide, *J. Mater. Chem. A* 8 (2020) 11773–11780.
- [12] W. Liu, C. Song, M. Kou, Y. Wang, Y. Deng, T. Shimada, L. Ye, Fabrication of ultrathin g-C<sub>3</sub>N<sub>4</sub> nanoplates for efficient visible-light photocatalytic H<sub>2</sub>O<sub>2</sub> production via two-electron oxygen reduction, *Chem. Eng. J.* 425 (2021), 130615.
- [13] Y. Zhao, Y. Liu, J. Cao, H. Wang, M. Shao, H. Huang, Y. Liu, Z. Kang, Efficient production of H<sub>2</sub>O<sub>2</sub> via two-channel pathway over ZIF-8/C<sub>3</sub>N<sub>4</sub> composite photocatalyst without any sacrificial agent, *Appl. Catal. B: Environ.* 278 (2020), 119289.
- [14] Z. Chen, D. Yao, C. Chu, S. Mao, Photocatalytic H<sub>2</sub>O<sub>2</sub> production Systems: design strategies and environmental applications, *Chem. Eng. J.* 451 (2023), 138489.
- [15] H. Zhu, Q. Xue, G. Zhu, Y. Liu, X. Dou, X. Yuan, Decorating Pt@cyclodextrin nanoclusters on C<sub>3</sub>N<sub>4</sub>/MXene for boosting the photocatalytic H<sub>2</sub>O<sub>2</sub> production, *J. Mater. Chem. A* 9 (2021) 6872–6880.
- [16] D. Zhu, G. Xu, M. Barnes, Y. Li, C.P. Tseng, Z. Zhang, J.J. Zhang, Y. Zhu, S. Khalil, M.M. Rahman, R. Verdusco, P.M. Ajayan, Covalent organic frameworks for batteries, *Adv. Funct. Mater.* 31 (2021) 2100505.
- [17] N. Huang, L. Zhai, D.E. Coupry, M.A. Addicoat, K. Okushita, K. Nishimura, T. Heine, D. Jiang, Multiple-component covalent organic frameworks, *Nat. Commun.* 7 (2016) 12325.
- [18] K. Xiong, Y. Wang, F. Zhang, X. Li, X. Lang, Linker length-dependent photocatalytic activity of  $\beta$ -ketonamine covalent organic frameworks, *Appl. Catal. B: Environ.* 322 (2023), 122135.
- [19] S. Yang, X. Li, T. Tan, J. Mao, Q. Xu, M. Liu, Q. Miao, B. Mei, P. Qiao, S. Gu, F. Sun, J. Ma, G. Zeng, Z. Jiang, A fully-conjugated covalent organic framework-derived carbon supporting ultra-close single atom sites for ORR, *Appl. Catal. B: Environ.* 307 (2022), 121147.
- [20] X. Zhao, P. Pachfule, A. Thomas, Covalent organic frameworks (COFs) for electrochemical applications, *Chem. Soc. Rev.* 50 (2021) 6871–6913.
- [21] H. Wang, H. Wang, Z. Wang, L. Tang, G. Zeng, P. Xu, M. Chen, T. Xiong, C. Zhou, X. Li, D. Huang, Y. Zhu, Z. Wang, J. Tang, Covalent organic framework photocatalysts: structures and applications, *Chem. Soc. Rev.* 49 (2020) 4135–4165.
- [22] M.S. Lohse, T. Bein, Covalent organic frameworks: structures, synthesis, and applications, *Adv. Funct. Mater.* 28 (2018) 1705553.
- [23] J. Wang, S. Zhuang, Covalent organic frameworks (COFs) for environmental applications, *Coord. Chem. Rev.* 400 (2019), 213046.
- [24] W.K. An, S.J. Zheng, X. Xu, L.J. Liu, J.S. Ren, L. Fan, Z.K. Yang, Y. Ren, C. Xu, Integrating benzofuran and heteroradialene into donor-acceptor covalent organic frameworks for photocatalytic construction of multi-substituted olefins, *Appl. Catal. B: Environ.* 316 (2022), 121630.
- [25] H. Cheng, H. Lv, J. Cheng, L. Wang, X. Wu, H. Xu, Rational design of covalent heptazine frameworks with spatially separated redox centers for high-efficiency photocatalytic hydrogen peroxide production, *Adv. Mater.* 34 (2022) 2107480.
- [26] Y. Zhang, J. Qiu, B. Zhu, M.V. Fedin, B. Cheng, J. Yu, L. Zhang, ZnO/COF S-scheme heterojunction for improved photocatalytic H<sub>2</sub>O<sub>2</sub> production performance, *Chem. Eng. J.* 444 (2022), 136584.
- [27] H. Cheng, J. Cheng, L. Wang, H. Xu, Reaction pathways toward sustainable photosynthesis of hydrogen peroxide by polymer photocatalysts, *Chem. Mater.* 34 (2022) 4259–4273.
- [28] X. Yu, B. Viengkeo, Q. He, X. Zhao, Q. Huang, P. Li, W. Huang, Y. Li, Electronic tuning of covalent triazine framework nanoshells for highly efficient photocatalytic H<sub>2</sub>O<sub>2</sub> production, *Adv. Sustain. Syst.* 5 (2021) 2100184.
- [29] H. Wang, C. Yang, F. Chen, G. Zheng, Q. Han, A crystalline partially fluorinated triazine covalent organic framework for efficient photosynthesis of hydrogen peroxide, *Angew. Chem. Int. Ed.* 61 (2022) 202202328.
- [30] L. Li, Z. Zhou, L. Li, Z. Zhuang, J. Bi, J. Chen, Y. Yu, J. Yu, Thioether-functionalized 2D covalent organic framework featuring specific affinity to Au for photocatalytic hydrogen production from seawater, *ACS Sustain. Chem. Eng.* 7 (2019) 18574–18581.
- [31] H. Pan, M. Sun, X. Wang, M. Zhang, M. Murugananthan, Y. Zhang, A novel electric-assisted photocatalytic technique using self-doped TiO<sub>2</sub> nanotube films, *Appl. Catal. B: Environ.* 307 (2022), 121174.
- [32] F.J. Uribe-Romo, C.J. Doonan, H. Furukawa, K. Oisaki, O.M. Yaghi, Crystalline covalent organic frameworks with hydrazone linkages, *J. Am. Chem. Soc.* 133 (2011) 11478–11481.
- [33] Y. He, X. Chen, C. Huang, L. Li, C. Yang, Y. Yu, Encapsulation of Co single sites in covalent triazine frameworks for photocatalytic production of syngas, *Chin. J. Catal.* 42 (2021) 123–130.
- [34] Z. Zhou, P. Li, X. Gao, J. Chen, K. Akhtar, E.M. Bakhsh, S.B. Khan, Y. Shen, M. Wang, Constructing two-dimensional heterojunction through decorating covalent organic framework with MoS<sub>2</sub> for enhanced photoelectrochemical water oxidation, *J. Environ. Chem. Eng.* 10 (2022), 106900.
- [35] W. Zhao, P. Yan, B. Li, M. Bahri, L. Liu, X. Zhou, R. Clowes, N.D. Browning, Y. Wu, J.W. Ward, A.I. Cooper, Accelerated synthesis and discovery of covalent organic framework photocatalysts for hydrogen peroxide production, *J. Am. Chem. Soc.* 144 (2022) 9902–9909.
- [36] Q. Jiang, L. Sun, J. Bi, S. Liang, L. Li, Y. Yu, L. Wu, MoS<sub>2</sub> quantum dots-modified covalent triazine-based frameworks for enhanced photocatalytic hydrogen evolution, *ChemSusChem* 11 (2017) 1108–1113.
- [37] S. Bhunia, S.K. Das, R. Jana, S.C. Peter, S. Bhattacharya, M. Addicoat, A. Bhaumik, A. Pradhan, Electrochemical stimuli-driven facile metal-free hydrogen evolution from pyrene-porphyrin-based crystalline covalent organic framework, *ACS Appl. Mater. Interfaces* 9 (2017) 23843–23851.
- [38] Z.B. Zhou, X.H. Han, Q.Y. Qi, S.X. Gan, D.L. Ma, X. Zhao, A facile, efficient, and general synthetic method to amide-linked covalent organic frameworks, *J. Am. Chem. Soc.* 144 (2022) 1138–1143.
- [39] M.P. Kou, Y.Y. Wang, Y.X. Xu, L. Ye, Y.P. Huang, B.H. Jia, H. Li, J. Ren, Y. Deng, J. Chen, Y. Zhou, K. Lei, L. Wang, W. Liu, H. Huang, T.Y. Ma, Molecularly engineered covalent organic frameworks for hydrogen peroxide photosynthesis, *Angew. Chem. Int. Ed.* 61 (2022) 202200413.
- [40] L. Chen, L. Wang, Y. Wan, Y. Zhang, Z. Qi, X. Wu, H. Xu, Acetylene and diacetylene functionalized covalent triazine frameworks as metal-free photocatalysts for hydrogen peroxide production: a new two-electron water oxidation pathway, *Adv. Mater.* 32 (2020) 1904433.
- [41] Q. Tian, L. Jing, S. Ye, J. Liu, R. Chen, C.H. Price, F. Fan, J. Liu, Nanospatial charge modulation of monodispersed polymeric microsphere photocatalysts for exceptional hydrogen peroxide production, *Small* 17 (2021) 2103224.
- [42] X. Zeng, Y. Liu, Y. Kang, Q. Li, Y. Xia, Y. Zhu, H. Hou, M.H. Uddin, T. R. Gengenbach, D. Xia, C. Sun, D.T. McCarthy, A. Deletic, J. Yu, X. Zhang, Simultaneously tuning charge separation and oxygen reduction pathway on graphitic carbon nitride by polyethylenimine for boosted photocatalytic hydrogen peroxide production, *ACS Catal.* 10 (2020) 3697–3706.
- [43] Z. Wei, M. Liu, Z. Zhang, W. Yao, H. Tan, Y. Zhu, Efficient visible-light-driven selective oxygen reduction to hydrogen peroxide by oxygen-enriched graphitic carbon nitride polymers, *Energy Environ. Sci.* 11 (2018) 2581–2589.
- [44] C. Chu, D. Huang, Q. Zhu, E. Stavitski, J.A. Spies, Z. Pan, J. Mao, H.L. Xin, C. A. Schmuttenmaer, S. Hu, J.H. Kim, Electronic tuning of metal nanoparticles for highly efficient photocatalytic hydrogen peroxide production, *ACS Catal.* 9 (2019) 626–631.
- [45] F.M. Zhang, J.L. Sheng, Z.D. Yang, X.J. Sun, H.L. Tang, M. Lu, H. Dong, F.C. Shen, J. Liu, Y.Q. Lan, Rational design of MOF/COF hybrid materials for photocatalytic H<sub>2</sub> evolution in the presence of sacrificial electron donors, *Angew. Chem. Int. Ed.* 57 (2018) 12106–12110.
- [46] Z. Zhou, C. Bie, P. Li, B. Tan, Y. Shen, A thioether-functionalized pyrene-based covalent organic framework anchoring ultrafine Au nanoparticles for efficient photocatalytic hydrogen generation, *Chin. J. Catal.* 43 (2022) 2699–2707.
- [47] L. Guo, Y. Niu, S. Razaque, B. Tan, S. Jin, Design of D-A1–A2 covalent triazine frameworks via copolymerization for photocatalytic hydrogen evolution, *ACS Catal.* 9 (2019) 9438–9445.
- [48] X. Zhang, P. Ma, C. Wang, L. Gan, X. Chen, P. Zhang, Y. Wang, H. Li, L. Wang, X. Zhou, K. Zheng, Unraveling the dual defect sites in graphite carbon nitride for ultra-high photocatalytic H<sub>2</sub>O<sub>2</sub> evolution, *Energy Environ. Sci.* 15 (2022) 830–842.
- [49] S. Fu, S. Yao, S. Guo, G.C. Guo, W. Yuan, T.B. Lu, Z.M. Zhang, Feeding carbonylation with CO<sub>2</sub> via the synergy of single-site/nanocluster catalysts in a photosensitizing MOF, *J. Am. Chem. Soc.* 143 (2021) 20792–20801.
- [50] N. Tian, Y. Zhang, X. Li, K. Xiao, X. Du, F. Dong, G. Waterhouse, T. Zhang, H. Huang, Precursor-reforming protocol to 3D mesoporous g-C<sub>3</sub>N<sub>4</sub> established by ultrathin self-doped nanosheets for superior hydrogen evolution, *Nano Energy* 38 (2017) 72–81.
- [51] D.N. Bunck, W.R. Dichtel, Bulk synthesis of exfoliated two-dimensional polymers using hydrazone-linked covalent organic frameworks, *J. Am. Chem. Soc.* 135 (2013) 14952–14955.
- [52] T. Zhou, S. Chen, L. Li, J. Wang, Y. Zhang, J. Li, J. Bai, L. Xia, Q. Xu, M. Rahim, B. Zhou, Carbon quantum dots modified anatase/rutile TiO<sub>2</sub> photoanode with dramatically enhanced photoelectrochemical performance, *Appl. Catal. B: Environ.* 269 (2020), 118776.
- [53] M. Sun, X. Wang, Z. Chen, M. Murugananthan, Y. Chen, Y. Zhang, Stabilized oxygen vacancies over heterojunction for highly efficient and exceptionally durable VOCs photocatalytic degradation, *Appl. Catal. B: Environ.* 273 (2020), 119061.